

Mechanical tomography of a volcano plumbing system from GNSS unsupervised modeling

François Beauducel^{1,2}, Aline Peltier^{1,3}, Antoine Villié⁴, Wiwit Suryanto⁵

⁴Institut de physique du globe de Paris, Université de Paris, CNRS, F-75005 Paris, France

⁵Institut des Sciences de la Terre, IRD UR 219, Yogyakarta 55166, Indonesia

⁶Observatoire Volcanologique du Piton de la Fournaise, IPGP, F-97418 La Plaine des Cafres, La Réunion

⁷Laboratoire de biométrie et biologie évolutive, CNRS UMR 5558, F-69622 Villeurbanne, France

⁸Geophysics Research Group, Universitas Gadjah Mada, Yogyakarta 55281, Indonesia

Key Points:

- imaging volcano plumbing system from geodesy and mechanical modeling
- detecting precursory magma migration and anticipating real erupted volume
- new unsupervised real-time modeling tool for volcano monitoring

13 **Abstract**

14 Identification of internal structures in an active volcano is mandatory to quantify the phys-
 15 ical processes preceding eruptions. We propose a fully unsupervised Bayesian inversion
 16 method that uses the point compound dislocation model as a complex source of defor-
 17 mation, to dynamically identify the substructures activated during magma migration.
 18 We applied this method at Piton de la Fournaise. Using 7-day moving trends of GNSS
 19 data preceding the June 2014 eruption, we compute a total of 15 inversion models of 2.5
 20 million forward problems each, without a priori information. Obtained source shapes (dikes,
 21 prolate ellipsoids or pipes) exhibit a global migration from 7–8 km depth to the surface,
 22 drawing a “mechanical tomography” of the plumbing system. Our results allow retriev-
 23 ing geometries compatible with observed eruptive fissures and seismicity distribution,
 24 and the retrieved source volume variations made this method a good proxy to anticipate
 25 erupted lava in case of no co-eruptive refilling.

26 **Plain Language Summary**

27 Imaging the interior of an active volcano and estimating volumes of magma in depth
 28 are major challenges of eruption anticipation and forecast. In this work we propose an
 29 effective method of data processing that combines a new analytical model of theoret-
 30 ical source, and standard ground deformation measurements, in a fully automated pro-
 31 cess. The method is sensitive to magma migration and behaves like a scanner that dis-
 32 plays a 3D image of the volcano plumbing system.

33 **1 Introduction**

34 Active volcano edifices might deform due to fluid migration and storage into their
 35 so-called plumbing system, an interconnected network of internal volumetric substruc-
 36 tures like reservoirs, conduits or sills/dikes (Tibaldi, 2015). Indeed, fluid dynamics into
 37 the plumbing system involves mechanical constraints (pressure, volume or stress vari-
 38 ations) that are applied on the internal boundaries of the medium, inducing deforma-
 39 tion and displacements that usually reach the free surface. This behavior highly depends
 40 on the medium rheology (Sparks et al., 2019), and deformation intensity can sometimes
 41 be much below the instrumental detection capability. Yet, monitoring volcano deforma-
 42 tion has been commonly used for more than half a century to detect the subtle warn-
 43 ing signals of a volcanic eruption linked to the pressurization of magma body or magma
 44 transfers at depth (see Dzurisin (2003) for a complete review and Segall (2010) for lim-
 45 itations of the deformation methods). In this context, the characterization of the magma
 46 feeding system (location, volume, shape, etc.) with short-term and reliable quantitative
 47 parameters is an important prerequisite for understanding and anticipating any erup-
 48 tive activity. Inversion of geodetic data with mechanical models has natural capability
 49 to locate the pressure source in depth and quantify its characteristics from surface ob-
 50 servations (see for instance Toutain et al. (1992); Cayol and Cornet (1998); Beauducel
 51 et al. (2004); Anderson et al. (2010); Peltier et al. (2016)). Moreover, any quantitative
 52 volcano model needs boundary conditions, in particular those common to the magma
 53 fluid dynamics and the volcano mechanical behavior, i.e., the plumbing system geom-
 54 etry. Imaging these structures using various tomography methods has the main goal of
 55 describing, in a more quantitative way than any geological approach, the internal struc-
 56 tures, which might be used in other geophysical or geochemical dynamic modeling as a
 57 priori information.

58 We propose, in this paper, to follow the magma circulation and/or accumulation
 59 by locating and quantifying pressurisation sources in space and time using unsupervised
 60 deformation source modeling from GNSS observations at Piton de la Fournaise (PdF).
 61 We introduce here the innovative term of “mechanical tomography”, since the method
 62 uses magma ascent as an active source that progressively “illuminates” the complex magma

63 plumbing system, and finally gives an image of the internal substructure geometries, which
64 have been activated during the PdF unrest.

65 PdF (La Réunion Island, Indian Ocean, Figure 1a) is an active basaltic volcano,
66 often in eruption with an average of 2 eruptions per year since 1979, date of the creation
67 of the Observatoire Volcanologique du Piton de la Fournaise (OVPF) from the Institut
68 de Physique du Globe de Paris. The recent eruptive activity mainly occurs inside an un-
69 inhabited caldera, called Enclos Fouqué, where a terminal cone topped by two craters
70 (Bory and Dolomieu), gradually built up (Figure 1b).

71 The location and the shape of the shallow magma reservoirs below the volcano are
72 still debated even if recent geodetic, seismic and geochemical studies converge on a global
73 scheme of a plumbing system constituted of several reservoirs, variably connected and
74 distributed from 10 km depth to the near-surface (Battaglia et al., 2005; Peltier et al.,
75 2009; Di Muro et al., 2014; Boudoire et al., 2019). Passive S and P-wave tomographies
76 made on PdF, using ambient seismic noise and P-wave first arrival times for earthquakes,
77 respectively, show 1) a high S-wave velocity zone from -1 to 1.9 km below the terminal
78 cone interpreted as a preferential paths for magma injections (Brenguier et al., 2007) and
79 2) a high-velocity plug at sea level, under the summit craters, interpreted as an intru-
80 sive, solidified dike-and-sill complex with little fluid magma storage (Prôno et al., 2009).
81 Two low P-wave velocity anomalies, which may highlight magma reservoirs, are found
82 from 0 to 1 km a.s.l. and from 1 to 2 km b.s.l. (Prôno et al., 2009). At greater depth,
83 spatio-temporal distribution of the seismicity located by OVPF may evidence the pres-
84 ence of a deeper reservoir at around 7.5 km depth below the Bory crater (Battaglia et
85 al., 2005; Peltier et al., 2009).

86 In June, 2014, after an unusual period of 41 months of dormancy, PdF showed signs
87 of unrest with the start of a slow edifice inflation and an increase of the shallow (± 2 km
88 depth) seismic activity on June 9. Two seismic crises (not associated with rapid ground
89 deformation) occurred on June 13 and 17, with 360 and 687 shallow volcano-tectonic earth-
90 quakes, respectively. A last seismic crisis that lasted one hour and 16 minutes (888 shal-
91 low volcano-tectonic earthquakes located between 0.3 and 1.5 km a.s.l. below the Dolomieu
92 crater; associated with rapid ground deformation) led to an eruption on June 20, 21:35
93 (UTC time). The eruptive fissures opened on the external and south south-eastern slope
94 of the Dolomieu crater (2348–2480 m elevation; Figure 1b). Eruptive activity ended on
95 June 21, 17:09 (UTC time) and emitted about 0.4 ± 0.2 million m³ of lava flows (no DRE).

96 2 Methods

97 2.1 GNSS Data Processing

98 Among other multidisciplinary networks, OVPF maintains 24 permanent GNSS
99 stations, one of the densest networks on an active volcano. For this study, we only used
100 the daily solutions of the 10 stations within a 4 km radius from the summit (Figure 1b),
101 where ground displacements have been significant during the June 2014 unrest (Figure
102 1c). Data shown in the paper were processed using PPP method by the Gipsy-Oasis soft-
103 ware (Desai et al., 2014) providing daily solutions in the ITRF2008 referential, with typ-
104 ical standard deviations of 5.2 mm, 4.8 mm, and 11.2 mm for eastern, northern and ver-
105 tical components, respectively, over 5 years period at a stable station in La Réunion. Hor-
106 izontal tectonic motion has been removed from the time series using linear trend values
107 of +17.9 mm/yr and +12 mm/yr for eastern and northern components, respectively.

108 In order to increase the signal to noise ratio of GNSS observations, we compute dis-
109 placement trends over a 7 days moving-window, which represents a good compromise be-
110 tween the constraint of the source shape and a detailed time tracking of the source. In-
111 deed, as the GNSS daily solutions have relatively high errors, the computation of a lin-
112 ear trend over a few days' sliding sample window increases the sensitivity to detect sub-

tle signals below the error level of individual daily solutions. Typically, the error on a 7-day velocity trend is as low as about 0.14 mm/day, i.e., only 0.8 mm on the displacement.

2.2 pCDM Method

The point compound dislocation model (pCDM) has been proposed by Nikkhoo et al. (2016). It provides analytical expressions for surface displacements due to a source composed of three mutually orthogonal tensile point dislocations, one horizontal and two vertical, freely oriented in space (three rotational degrees of freedom around each 3D axis) in an elastic homogeneous half-space. Original equations depend on nine source parameters: three for the hypocenter location (horizontal coordinates and depth), three volume variations dV_X , dV_Y and dV_Z (of the same sign, for each plane perpendicular to its axis), and three for the angles of rotations Ω_X , Ω_Y , Ω_Z (see Figure 2). A tenth parameter is the Poisson's ratio that we fixed to 0.25 to consider an isotropic medium. Since equations use the volume dislocation for the deformation source and not the pressure, the model is independent from other elastic parameters.

In order to express the total volume dislocation ΔV , an easier quantitative parameter for interpretation, we substituted the three volume variations variables with their total value plus two dimensionless shape ratios between 0 and 1, defined as follows:

$$\Delta V = dV_X + dV_Y + dV_Z, \quad (1)$$

$$A = \frac{dV_Z}{\Delta V}, \quad (2)$$

$$B = \frac{dV_Y}{dV_X + dV_Y}, \quad (3)$$

where ΔV is the total volume variation of the source, A is the horizontal over total volume variation ratio, and B is the vertical volume variation ratio.

The pCDM is able to approximate any shape of magma bodies, as dikes, sills, oblate, prolate and other triaxial ellipsoidal shapes (see some examples with corresponding A and B values in Figure 2), and is only relevant at far-field observation points because of the point source approximation. Even if simple, this model is particularly well adapted for real-time monitoring as it gives a first order estimation of the magnitude and shape characteristics of the source(s) at the origin of the surface displacements, and is still easy to implement in an inverse problem.

We also rewrote the original pCDM code in a fully vectorized way (Matlab/GNU Octave and C languages) in order to make it compatible with fast inversion and millions of forward problems. Furthermore, vectorization allows using equations with the varying-depth formulation to approximate the topographic effects (Williams & Wadge, 1998; Beauducel & Carbone, 2015), i.e., adjusting the source depth at each observation point using station elevation above sea level. This method is also a good way to solve the eternal problem of source elevation referencing in half-space models: here the source depths are given in meters b.s.l..

2.3 Inverse Problem

In order to obtain a description as objective as possible of the volcano internal structures at the origin of the surface displacements, we minimize the a priori information and explore the entire space of the nine model parameters using the GNSS trends as observation data. As a first result of this unsupervised inversion method, we represent the model space probability as a function of source location, in order to display all solutions that

154 are consistent with observations (Tarantola, 2006). Identification of a single volume zone
 155 with higher probabilities confirms the existence of a cluster of good models, a manda-
 156 tory condition to possibly select one “best model”.

157 Since exhaustive grid exploration of the full model space is not reasonable with 9
 158 parameters, we use a Monte Carlo Bayesian parallel algorithm with 5 iterations, each
 159 using 500,000 forward problems randomly chosen in the 9-parameters model space, and
 160 possible reduction of any parameter search interval between iterations. The aim of this
 161 algorithm is to drastically reduce the relevant range of variation for each parameter, with
 162 a low probability to exclude the best model. Each iteration performs uniform sampling
 163 of the 9 parameters except for horizontal position for which we use a normally distributed
 164 sampling centered at the summit with a 5-km standard deviation radius. This a priori
 165 information improves the inversion performance as we are expecting source in the neigh-
 166 borhood of the summit area, but does not exclude any possible distant nor deep source
 167 location. Then it computes the misfits associated with the created models, using the L1
 168 norm between observed and computed data, and draws the curve representing a proxy
 169 of the best possible misfit as a function of the parameter value. If the misfit distribu-
 170 tion has a single significant maximum probability mode, the process selects a smaller range
 171 for this parameter with higher probability to constrain the best models. This new in-
 172 terval will be used as a starting point for the next iteration. A posteriori uncertainties
 173 of the best model solution are given by the interval of variation over each parameter that
 174 keeps 68% (one standard deviation) of the highest model probabilities for all the iter-
 175 ations, a total of 2.5 millions forward models.

176 3 Results

177 The long-term pre-eruptive edifice inflation is often of very low intensity at PdF
 178 (often less than 5 cm; e.g. in (Peltier et al., 2016, 2018), that is why we look at baseline
 179 changes (i.e. linear distance between pairs of stations) to better highlight changes in the
 180 deformation trend. After 41 months of rest and slow deflation, first signs of edifice in-
 181 flation at PdF appeared on June 9, 2014 (Figure 1c,d), and accelerated after June 13,
 182 with a summit extension well visible on the DSRG-SNEG baseline (see dark red lines
 183 in Figure 1d). Intensity of the ground deformation preceding the June 20, 2014 erup-
 184 tion remained particularly low, i.e. less than 1 cm of horizontal cumulative displacements
 185 and about 2 cm maximum of vertical cumulative displacements recorded on the sum-
 186 mit stations in 11 days. These low intensity of surface observations makes this eruption
 187 a good case study for developing sensitive modeling methods.

188 Results of the inversion modeling on 15 periods (12 before and 3 after the erup-
 189 tion) of 7 day sliding sample window allow retrieving the position and the shape of the
 190 pressure source at different times. Figure 3 shows results of each inversion as a full de-
 191 scription of the model space probabilities in horizontal and vertical projections (see also
 192 Table S1 in the supporting information). Three distinct pre-intrusion phases (phases 1-
 193 3) before the final dike propagation to the surface (phase 4) can be distinguished.

194 1) For the periods spanning June 2-8, 3-9, 4-10 and 5-11, no well-constrained source
 195 can be found but probable deep deflation diffuse sources seem to be present below the
 196 terminal cone.

197 2) Inflation sources appeared and became more consistent from the June 6-12 pe-
 198 riod with a narrower range of models and a best model in inflation located at 4.5 km be-
 199 low sea level, i.e. about 7 km below the summit, with a tilted dike shape. The inflation
 200 pressure source, the shape of which evolves from a dike to a pipe, remained deep (0 to
 201 3 km below sea level) until June 16.

202 3) From the June 11-17 to the June 13-19 periods, when the deformation rate ac-
 203 celerated, the inflation source was shallower, located between 0.7 and 1 km a.s.l. (i.e. be-

204 between 1.8 and 1.5 km below the summit). The last pressure source modelled before the
 205 eruption, for the period spanning June 13 to June 19, displayed a volume variation of
 206 +210,000 m³.

207 4) On June 20, a rapid (1 hour and 16 min of seismic crisis with rapid ground de-
 208 formation; Figure 1c) and final magma dike injection propagated to the surface and fed
 209 the eruption. The shape of the dike appeared in our models only from the June 16-22
 210 sliding-window. For the two previous periods including the beginning of the eruption (June
 211 14-20 and June 15-21), the best models were ellipsoid sources, probably because of the
 212 influence of two sources (the pre-eruptive source and the final dike reaching the surface)
 213 associated with the integrating effect of the 7-day trend calculation. Volume variations
 214 for the two last co-eruptive periods (15-21) and (16-22) were relatively constant, with
 215 values of +230,000 m³ and +300,000 m³, respectively.

216 4 Discussion

217 Even with very small ground displacements (less than 1 cm), we are able to im-
 218 age the refilling of the shallow magma plumbing system preceding the June 2014 erup-
 219 tion at PdF. Our previous attempts to detect pre-eruptive magma migration using de-
 220 formation data may have failed because of the use of too simple isotropic sources as pri-
 221 mary models (Beauducel et al., 2014). Success of the inversion using more complex sources
 222 may evidence the more frequent deformation sources with flat or elongated shape, like
 223 dikes or pipes at PdF.

224 Our results highlight from June 12 overpressures inside this system at decreasing
 225 depth with time (Figure 4), from 7 – 8 km b.s.l. (at the lower limit of our model space)
 226 where a reservoir has already been suggested by seismicity in 1998 (Battaglia et al., 2005),
 227 to 1.5 km a.s.l., where the shallower reservoir is supposed to lie (1.3 – 1.9 km depth be-
 228 low the summit (Peltier et al., 2016)). Most of the pressure sources below sea level are
 229 vertically elongated and seems to highlight the volcano deep conduit connecting the two
 230 reservoirs, forming a continuum more or less filled by fluids (Figures 3,4). Rather than
 231 following a clear magma migration, which may have required a higher time sampling fre-
 232 quency, we were able to deliver a mechanical tomography of the PdF plumbing system
 233 (from about 10 km depth to the surface; Figure 4). The synthetic 3D view of the dif-
 234 ferent sources identified during the June 2014 pre-eruptive unrest evidences a gap at sea
 235 level, at the same level where Prôno et al. (2009) describe high-velocity plug interpreted
 236 as a solidified complex with little fluid storage, and where Battaglia et al. (2005) describe
 237 a discontinuity in the upward migration of the seismicity preceding the 1998 eruption,
 238 which occurred after 6 years of rest. In June 2014, no deep seismicity was recorded dur-
 239 ing the upward magma migration. Following the 1998 eruption, most of the deep recharges
 240 were not accompanied by deep seismicity, and the majority of the earthquakes are lo-
 241 cated above sea level (Lengliné et al., 2016; Duputel et al., 2019). This is the sign of a
 242 more or less deep open conduit, which fed the 34 eruptions that occurred between 1998
 243 and 2014 (Roult et al., 2012). Our results show thus the importance of the method we
 244 used, which makes it possible to see what seismology does not when the system is already
 245 open. Thus, the first models (phase 1) show deep deflation sources before the deep magma
 246 migration starts (Figures 3,4). This volume loss might correspond to the emptying of
 247 a deeper reservoir(s) before the magma starts to "drill" and follows a path to shallower
 248 levels (phase 2; Figure 4). Source locations during phase 3 suggests that the fracturing
 249 that allows magma to reach the surface (phase 4) started from about 1.5 km depth be-
 250 low the southern border of the Dolomieu crater (Figures 3,4). The two seismic crises,
 251 on June 13 and 17, with earthquakes above sea level, show already shallow pressure source(s)
 252 at that time.

253 The estimated source volume variations are relatively stable during phases 3 and
 254 4, i.e. around 0.25 Mm³ (see Figure 3) despite the displacement increase over one order

of magnitude between pre- and co-eruptive periods. This volume stability makes sense as it might translate a finite volume of magma involved in the last magma migration process. However, when using an isotropic source this process cannot be properly modeled, as for a given depth, the volume variation must be proportional to surface displacements. Using pCDM, the source shape has the capability to be adjusted while keeping a constant volume variation and maintaining a shallow depth. In addition, the final volume variation is of the same order of magnitude as the one obtained using an isotropic source for the whole co-eruptive period (130.000 to 190.000 m³ (Peltier et al., 2016)), and close to the real erupted volume of 0.4±0.2 Mm³, i.e. a DRE volume of 0.17-0.28 assuming a porosity range of 30–58% (Di Muro et al., 2014).

In spite of the elastic and homogeneous assumptions of the models, adequacy of the volume variation obtained from deformation and erupted volume seems consistent with the case of short eruptions during which no long-term refilling occurred as for the June 2014 eruption. We demonstrate with our modelling the need of looking at shorter time periods to evidence migration processes and complex internal shallow structures. GNSS daily solutions are certainly a limitation in this context, and higher frequency may help in identification of finer structures.

5 Conclusion

The low intensity of surface observations preceding the June 20, 2014 eruption at PdF makes this eruption a good case study for developing and validating sensitive modeling methods. Our work provides good insights into the refilling of the shallow magma reservoir the days preceding the eruption. The pCDM method we used allows tracking the gradual migration of the magma to the upper reservoir, and the final dike propagation to the surface, by discriminating both the shape, location and volume of the source. The rewriting of the original pCDM code in a fully vectorized way allows for fast inversion and is easy to implement to give first-order modelling results, helpful notably for crisis management. With similar results as obtained at Mt. Etna by Cannavò et al. (2015), our method is fast and fully unsupervised, without a priori information on the source parameters except the choice of the pCDM itself. In view of these promising results, we implemented the method as an extension of the GNSS module in the WebObs system, an integrated web-based system for data monitoring and network management, implemented in 15 observatories worldwide (Beauducel et al., 2020). The module was initially developed with a simple isotropic point source (Beauducel et al., 2014, 2019) and we added the possibility of setting a pCDM source and associated parameters for real-time modeling. This has been especially useful during recent crisis managements (Moretti et al., 2020; Peltier et al., 2020).

Acknowledgments

This work is a tribute to FB's late thesis supervisor François H. Cornet. Authors warmly thank Mehdi Nikkhoo for sharing his revolutionary analytical model. Many thanks to the University of Gajah Mada, the IRD in Jakarta and the Indonesian Ministry RistekDikti for having supported the project. We thank the OVPF staff for high quality data collection. GNSS raw data are available at <http://volobsis.ipgp.fr>, processed data by contacting OVPF-IPGP. WebObs system is an open-source project available at <https://github.com/IPGP/webobs>. This work has been funded by the Observatoire des Sciences de l'Univers de Grenoble and EUROVOLC project that received funding from the European Union's Horizon 2020 research and innovation programme under grant agreement No 731070. IPGP contribution XXXX.

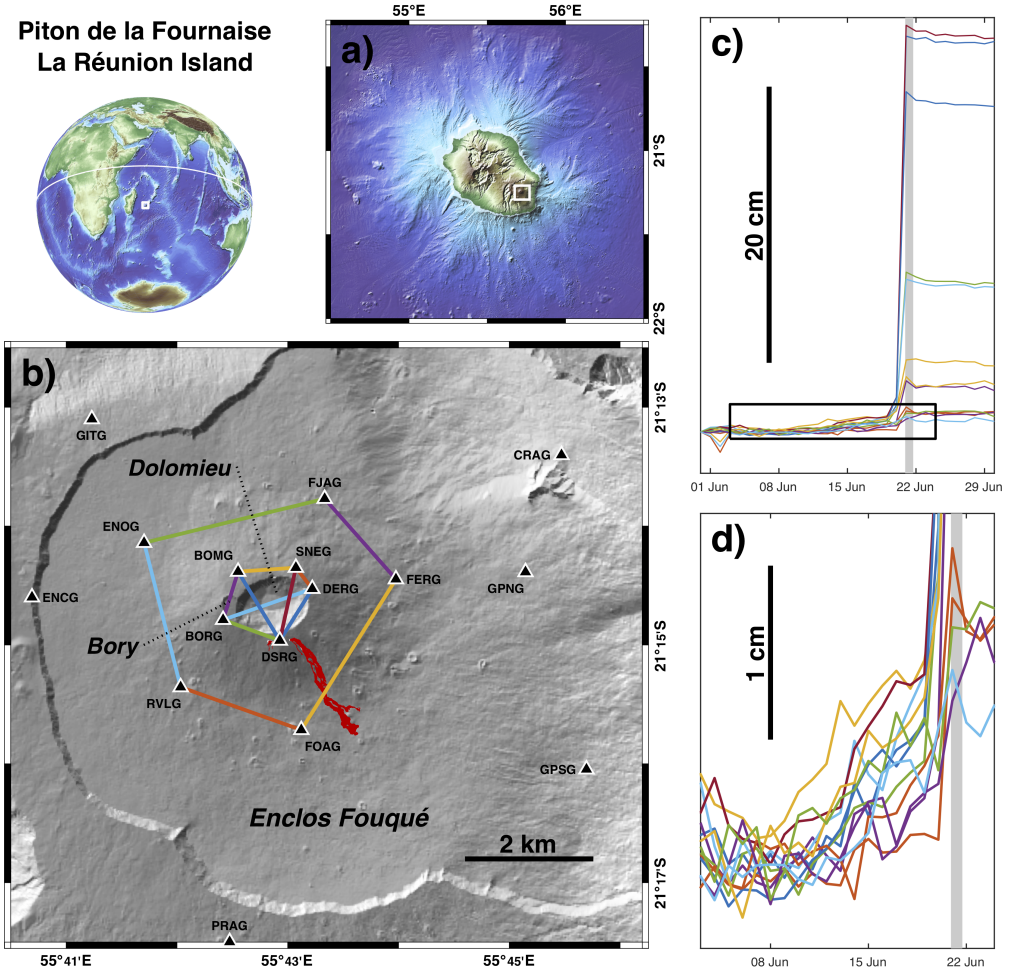


Figure 1. a) Location map of La Réunion Island; b) Zoom on the most active part of Piton de la Fournaise and summit craters. GNSS permanent stations (black triangles), June 2014 lava flows (solid red patch), and selected baselines (color solid lines) are shown; c) baseline variations (i.e. distance changes between pairs of stations) on the pre-, co-, and post-eruptive periods (same colors as in b); d) zoom on the pre-eruptive precursory baseline variations. Grey area indicates eruption time. Topographic data from ETOPO1, SRTM, SHOM, and RGEALTI © IGN 2016.

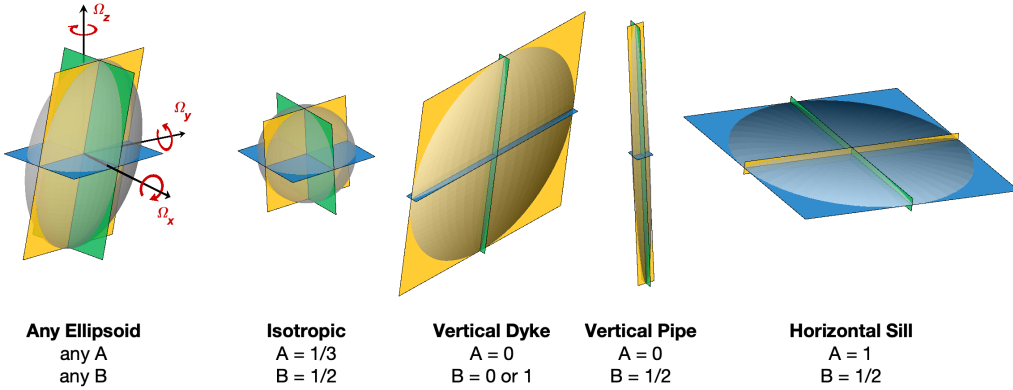


Figure 2. pCDM dislocation plans and rotation angles definition. Example of source shapes and the associated A and B values. Surface of each point dislocation is enlarged to be proportional to its associated volume variation.

References

- Anderson, K., Lisowski, M., & Segall, P. (2010). Cyclic ground tilt associated with the 2004–2008 eruption of Mount St. Helens. *Journal of Geophysical Research: Solid Earth*, 115(B11).
- Battaglia, J., Ferrazzini, V., Staudacher, T., Aki, K., & Cheminée, J.-L. (2005). Pre-eruptive migration of earthquakes at the Piton de la Fournaise volcano (Réunion Island). *Geophysical Journal International*, 161(2), 549–558.
- Beauducel, F., & Carbone, D. (2015). A strategy to explore the topography-driven distortions in the tilt field induced by a spherical pressure source: the case of mt etna. *Geophysical Journal International*, 201(3), 1471–1481.
- Beauducel, F., De Natale, G., Obrizzo, F., & Pingue, F. (2004). 3-D modelling of Campi Flegrei ground deformations: An example of trade-off between source and structure. *Pure Appl. Geophys.*, 161(7), 1329–1344.
- Beauducel, F., Lafon, D., Béguin, X., Saurel, J.-M., Bosson, A., Mallarino, D., ... Fahmi, A. A. (2020). WebObs: The volcano observatories missing link between research and real-time monitoring. *Frontiers in Earth Sciences*, 8, 48.
- Beauducel, F., Nandaka, M. A., Syahbana, D. K., Suryanto, W., Nurnaning, A., Iguchi, M., ... Komorowski, J.-C. (2019). Real-time magma flux quantization from GNSS as a tool for crisis management. In *VOBP4, Mexico City, November 2019*.
- Beauducel, F., Nurnaning, A., Iguchi, M., Fahmi, A. A., Nandaka, M. A., Sumarti, S., ... Métaxian, J.-P. (2014). Real-time source deformation modeling through GNSS permanent stations at Merapi volcano (Indonesia). In *AGU Fall Meeting Abstracts*.
- Boudoire, G., Brugier, Y.-A., Di Muro, A., Wörner, G., Arienzo, I., Metrich, M., ... Pichavant, M. (2019). Eruptive activity on the western flank of Piton de la Fournaise (La Réunion Island, Indian Ocean): insights on magma transfer, storage and evolution at an oceanic volcanic island. *Journal of Petrology*, 5.

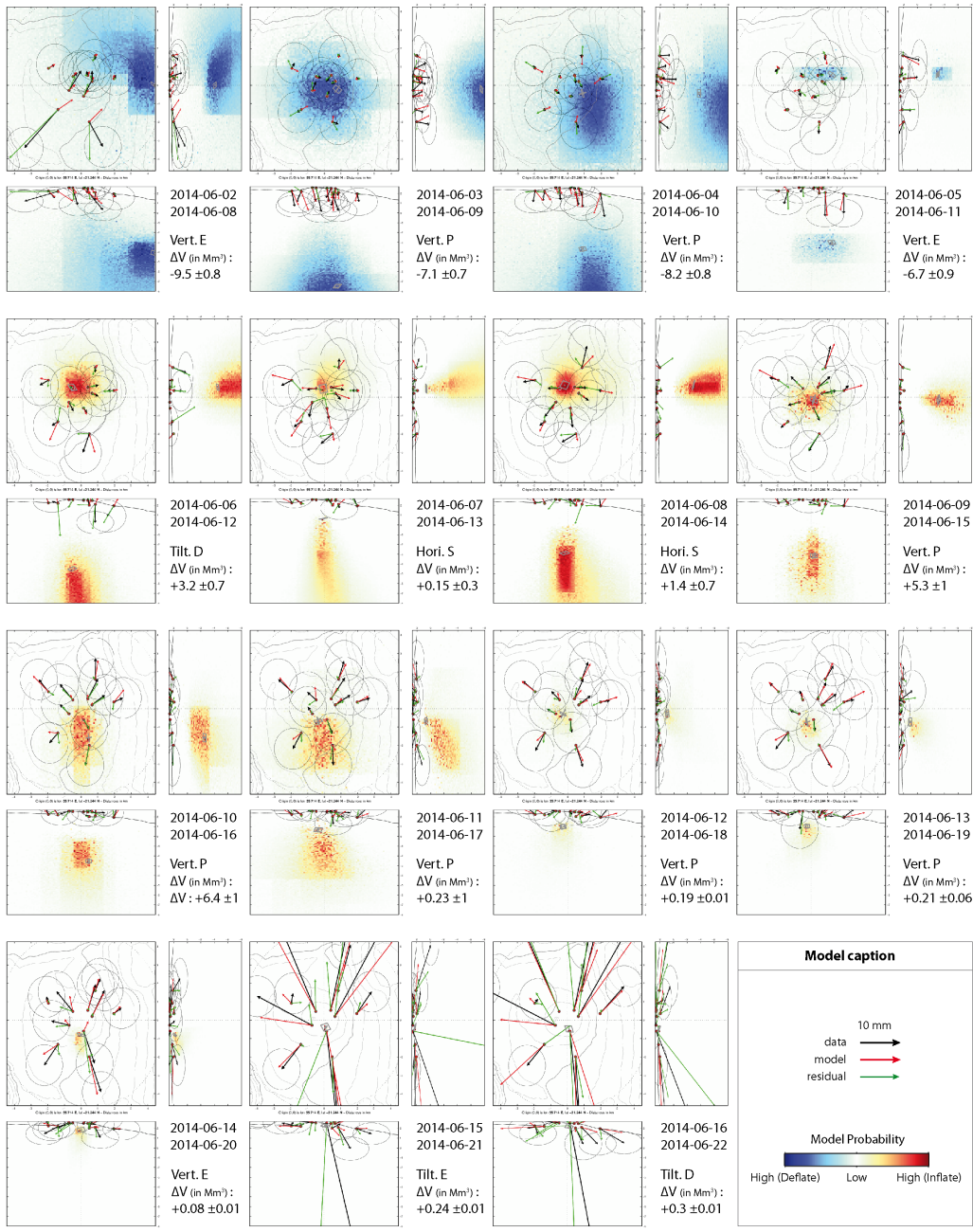


Figure 3. Temporal evolution of the daily pCDM source solution from Bayesian inversion of 7-day displacement trends from June 8 to 22, 2014, in map and vertical cross-section views. Time interval of each model is given in the figure. Color map indicates the maximum probability level combined with the volume variation sign (yellow-orange-red for inflation, green-cyan-blue for deflation). Black, red and green arrows are observed displacements, modeled displacements and residual, respectively. Ellipses are errors. Best model source location and shape are indicated as grey plans, and their source approximate shape (E: Ellipsoid, S: Sill, P: Pipe, D: Dike) and volume variation (Mm^3) are indicated.

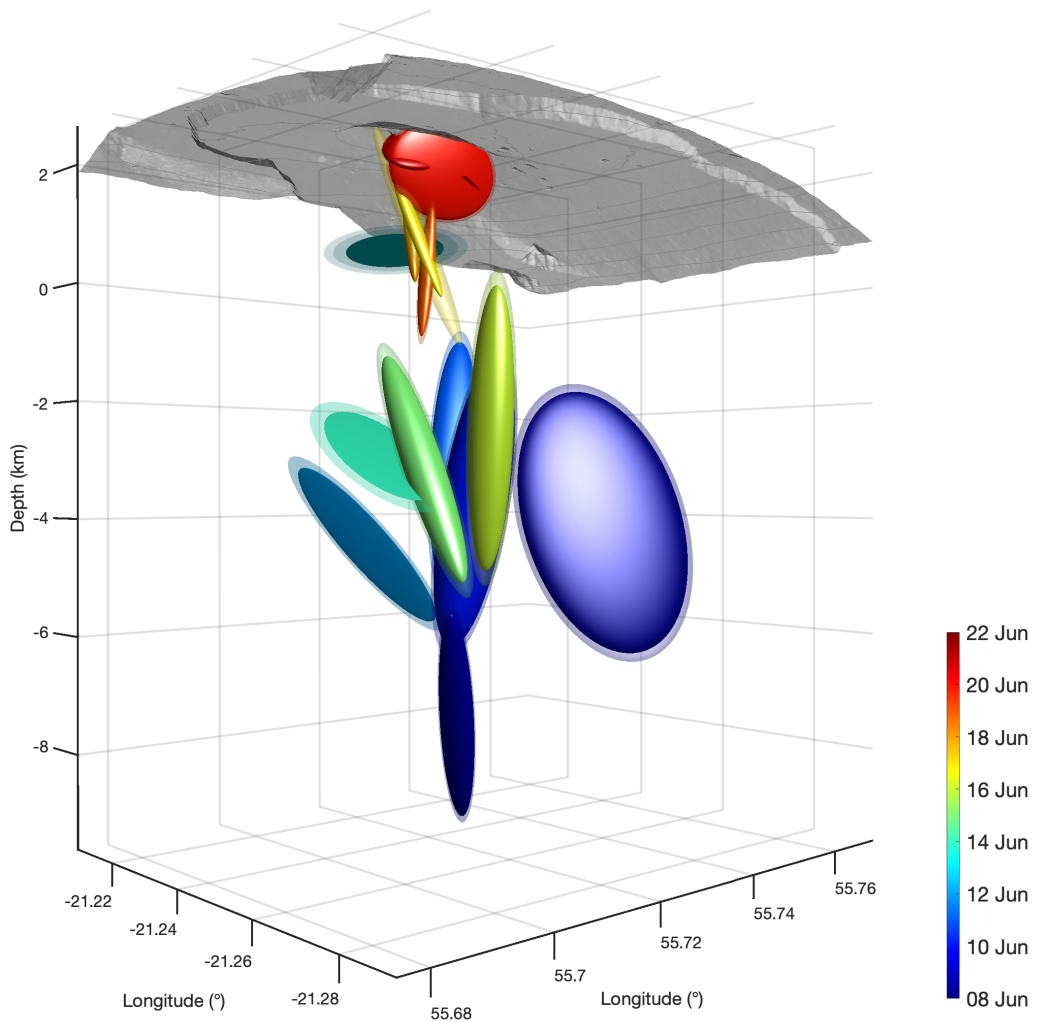


Figure 4. Synthetic and virtual 3D view of the different best models identified during the June 2014 pre-eruptive unrest at Piton de la Fournaise. Colors stand for the most recent date of each time window. Size of each source is proportional to its associated volume variation.

- 330 Brenguier, F., Shapiro, N. M., Campillo, M., Nercessian, A., & Ferrazzini, V. (2007).
 331 3-D surface wave tomography of the Piton de la Fournaise volcano using seis-
 332 mic noise correlations. *Geophysical research letters*, 34(2).
- 333 Cannavò, F., Camacho, A. G., González, P. J., Mattia, M., Puglisi, G., &
 334 Fernández, J. (2015). Real time tracking of magmatic intrusions by means
 335 of ground deformation modeling during volcanic crises. *Scientific reports*, 5,
 336 10970.
- 337 Cayol, V., & Cornet, F. H. (1998). Three-dimensional modeling of the 1983–1984
 338 eruption at Piton de la Fournaise Volcano, Réunion Island. *Journal of Geo-*
 339 *physical Research: Solid Earth*, 103(B8), 18025–18037.
- 340 Desai, S., Bertiger, W., Garcia-Fernandez, M., Haines, B., Murphy, D., Selle, C., ...
 341 Weiss, J. (2014). Status and plans at the JPL IGS analysis center. In *Intl.*
 342 *gnss service 2014 workshop compendium*, ed. igs central bureau (p. 53).
- 343 Di Muro, A., Métrich, N., Vergani, D., Rosi, M., Armienti, P., Fougeroux, T., ...
 344 Civetta, L. (2014). The shallow plumbing system of piton de la fournaise
 345 volcano (la reunion island, indian ocean) revealed by the major 2007 caldera-
 346 forming eruption. *Journal of Petrology*, 55(7), 1287–1315.
- 347 Duputel, Z., Lengliné, O., & Ferrazzini, V. (2019). Constraining spatio-temporal
 348 characteristics of magma migration at Piton De La Fournaise volcano from
 349 pre-eruptive seismicity. *Geophysical research letters*, 46(1), 119–127.
- 350 Dzurisin, D. (2003). A comprehensive approach to monitoring volcano deforma-
 351 tion as a window on the eruption cycle. *Rev. Geophys.*, 41(1). doi: 10.1029/
 352 2001RG000107
- 353 Lengliné, O., Duputel, Z., & Ferrazzini, V. (2016). Uncovering the hidden sig-
 354 nature of a magmatic recharge at Piton de la Fournaise volcano using small
 355 earthquakes. *Geophysical Research Letters*, 43(9), 4255–4262.
- 356 Moretti, R., Komorowski, J.-C., Ucciani, G., Moune, S., Jessop, D., de Chabalier,
 357 J.-B., ... Chaussidon, M. (2020). The 2018 unrest phase at La Soufrière of
 358 Guadeloupe (French West Indies) andesitic volcano: Scrutiny of a failed but
 359 prodromal phreatic eruption. *J. Volcanol. Geotherm. Res.*, 393, 106769. doi:
 360 10.1016/j.jvolgeores.2020.106769
- 361 Nikkhoo, M., Walter, T. R., Lundgren, P. R., & Prats-Iraola, P. (2016). Compound
 362 dislocation models (CDMs) for volcano deformation analyses. *Geophysical*
 363 *Journal International*, ggw427.
- 364 Peltier, A., Bachèlery, P., & Staudacher, T. (2009). Magma transport and storage
 365 at Piton de La Fournaise (La Réunion) between 1972 and 2007: A review of
 366 geophysical and geochemical data. *Journal of Volcanology and Geothermal*
 367 *Research*, 184(1-2), 93–108.
- 368 Peltier, A., Beauducel, F., Villeneuve, N., Ferrazzini, V., Di Muro, A., Aiuppa, A.,
 369 ... Taisne, B. (2016). Deep fluid transfer evidenced by surface deformation
 370 during the 2014–2015 unrest at Piton de la Fournaise volcano. *Journal of*
 371 *Volcanology and Geothermal Research*, 321, 140–148.
- 372 Peltier, A., Ferrazzini, V., Di Muro, A., Kowalski, P., Villeneuve, N., Richter, N., ...
 373 Gurrieri, S. (2020). Volcano crisis management at Piton de la Fournaise (La
 374 Réunion) during the COVID-19 lockdown. *submitted to Seismological Research*
 375 *Letters*.
- 376 Peltier, A., Villeneuve, N., Ferrazzini, V., Testud, S., Hassen Ali, T., Boissier, P., &
 377 Catherine, P. (2018). Changes in the long-term geophysical eruptive precursors
 378 at Piton de la Fournaise: Implications for the response management. *Frontiers*
 379 *in Earth Science*, 6, 104.
- 380 Prôno, E., Battaglia, J., Monteiller, V., Got, J.-L., & Ferrazzini, V. (2009). P-wave
 381 velocity structure of Piton de la Fournaise volcano deduced from seismic data
 382 recorded between 1996 and 1999. *Journal of Volcanology and Geothermal*
 383 *Research*, 184(1-2), 49–62.
- 384 Roult, G., Peltier, A., Taisne, B., Staudacher, T., Ferrazzini, V., Di Muro, A., &

- 385 OVPF, t. (2012). A new comprehensive classification of the Piton de la
386 Fournaise activity spanning the 1985–2010 period. Search and analysis of
387 short-term precursors from a broad-band seismological station. *Journal of*
388 *Volcanology and Geothermal Research*, 241, 78–104.
- 389 Segall, P. (2010). *Earthquake and volcano deformation*. Princeton Univ. Press.
- 390 Sparks, R., Annen, C., Blundy, J., Cashman, K., Rust, A., & Jackson, M. (2019).
391 Formation and dynamics of magma reservoirs. *Philosophical Transactions of*
392 *the Royal Society A*, 377(2139), 20180019.
- 393 Tarantola, A. (2006). Popper, Bayes and the inverse problem. *Nature physics*, 2(8),
394 492–494.
- 395 Tibaldi, A. (2015). Structure of volcano plumbing systems: A review of multi-
396 parametric effects. *Journal of Volcanology and Geothermal Research*, 298,
397 85–135.
- 398 Toutain, J.-P., Bachelery, P., Blum, P., Cheminée, J., Delorme, H., Fontaine, L., ...
399 Taochy, P. (1992). Real time monitoring of vertical ground deformations dur-
400 ing eruptions at Piton de la Fournaise. *Geophys. Res. Lett.*, 19(6), 553–556.
- 401 Williams, C., & Wadge, G. (1998). The effects of topography on magma chamber
402 deformation models: application to Mt. Etna and radar interferometry. *Geo-*
403 *phys. Res. Lett.*, 25(10), 1549–1552.